Research Article Vol. 37, No. 12 / December 2020 / Journal of the Optical Society of America A 1907

Journal of the Optical Society of America A

OPTICS, IMAGE SCIENCE, AND VISION

Numerical solution to the time-independent inhomogeneous photoacoustic wave equation using the Born series methods

Ratan K. Saha

Department of Applied Sciences, Indian Institute of Information Technology Allahabad, Jhalwa, Allahabad 211015, India (ratank.saha@iiita.ac.in)

Received 10 July 2020; revised 28 September 2020; accepted 27 October 2020; posted 27 October 2020 (Doc. ID 402471); published 18 November 2020

The traditional Born series (TBS) and convergent Born series (CBS) methods to numerically solve the time-independent inhomogeneous photoacoustic (PA) wave equation are discussed. The performance of these algorithms is examined for a circular PA source (a disk of radius, $a = 5$ μm) in two dimensions. The speed of sound within the source region was gradually decreased from $v_s = 1950$ to 1200 m/s, but the same quantity for the ambient medium was fixed to $v_f = 1500$ m/s. The PA fields were calculated over a large frequency band from $f = 7.3$ to 2000 MHz. Accordingly, the wave number ($k_f = 2\pi f/v_f$) varied from $k_f = 0.03$ to 8.38 μm^{-1}. The TBS method does not offer converging solutions when $k_f a \geq 25$ for $v_s = 1950$ m/s and $k_f a \geq 9$ for $v_s = 1200$ m/s. These have been observed in both the near and far fields. However, the solutions for the CBS technique converge in all cases. Both methods facilitate accurate solutions if the computational domain contains a collection of monodisperse/polydisperse disks considered in this study. Our numerical results suggest that the CBS protocol can provide accurate solutions under various test conditions.

https://doi.org/10.1364/JOSAA.402471

1. INTRODUCTION

The solutions to the inhomogeneous Helmholtz equation have found many applications in practice, spanning from seismology to electron scattering [1]. Analytic solutions can easily be derived for simple geometries such as spheroidal particles and infinite cylinders [2,3]. However, this equation, when applied to model practical problems, needs to be solved numerically because the shapes of the sources/scatterers are generally irregular. The commonly employed numerical schemes include finite difference time domain, pseudo-spectral time domain, and finite element methods, etc. Another class of techniques obtains solutions by iteratively solving integral equations via the Green's function method [4]. The famous traditional Born series (TBS) method belongs to this class. It is well known that the TBS procedure provides converging solutions for small particles and small scattering potential problems, but it fails to converge if particle size and scattering potential are large. Osnabrugge *et al*. have recently developed a method to address this issue, and it is referred to as the convergent Born series (CBS). It is derived by introducing a preconditioner into the TBS expression [5]. The CBS can provide converging solutions for the inhomogeneous Helmholtz equation in arbitrarily large media [5,6].

The time-independent photoacoustic (PA) wave equation converts into an inhomogeneous Helmholtz equation if the terms arising out of mismatch in the speed of sound of the source region with respect to the ambient medium are retained. This equation can be easily solved analytically for simple shapes [7]. Numerical solutions can be calculated for objects with arbitrary shapes using the k-Wave toolbox, which implements a pseudo-spectral method [8]. Natalie *et al*. proposed a transfer function approach to solve inhomogeneous problems in PAs, and also performed image reconstructions [9,10]. We have recently deployed the Born series methods to solve the inhomogeneous PA wave equation [11]. Our numerical study in two dimensions revealed that the TBS method fails to converge when the variation in the speed of sound is approximately $>22\%$ or $< -11\%$ of the source region with respect to the ambient medium. The CBS method provides the required robust numerical solution even in case of mismatch in the speed of sound in various regions of the computational domain. Though the methods have been examined for PAs, they can also be applied to solve similar problems in acoustics. In other words, the numerical results would be equally valid for a broad range of acoustic studies.

The Born series methods may be utilized to accurately calculate the PA fields generated by normal and deformed red blood cells (RBCs) for which the speed of sound mismatch with respect to saline water is about 10%. Previously, we calculated PA fields generated by normal and pathological RBCs using the Green's function method [12–14]. However, we did not consider acoustic inhomogeneity of the source in these studies.

The purpose of this work is to rigorously and quantitatively evaluate the roles of various parameters of the Born series methods as well as to assess the performance of these methods under different situations. For example, this study demonstrates (i) how the PA field expands with iteration, (ii) how the solutions behave in the near as well as in the far fields, (iii) what patterns the TBS and CBS methods follow for convergence, (iv) how mismatch in the density of the source region compared to the surrounding medium influences the solution, (v) what would happen when multiple sources are present in the computational domain, etc. It has been shown that the TBS method can handle various situations encountered in practice, but CBS further extends the validity domain.

The presentation of the paper is as follows. In Section 2, we derive the expressions for the PA field in the exact, TBS, and CBS techniques. The numerical methods are detailed in Section 3 and discussed in Section 4. A discussion and conclusions of this study are offered in Section 5.

2. THEORETICAL FRAMEWORK

A. Exact Solution

The detailed derivations of various approaches can be found in [11]. However, the theoretical framework is briefly mentioned here for the sake of completeness. Consider an acoustically inhomogeneous (compared to the surrounding medium) region containing uniformly distributed chromophores. It is illuminated by a pulsed laser light, and thus produces the PA waves due to thermo-elastic expansion. The well-known PA wave equations in the frequency domain can be cast as [7]

$$\nabla^2\psi(\mathbf{r}) + k_s^2\psi(\mathbf{r}) = \frac{i\omega\mu\beta I_0}{C_P}, \text{ within the source,} \tag{1a}$$

$$\nabla^2\psi(\mathbf{r}) + k_f^2\psi(\mathbf{r}) = 0, \text{ in the surrounding medium,} \tag{1b}$$

where μ, β, and C_P are the optical absorption coefficient, isobaric thermal expansion coefficient, and specific heat for the absorbing region, respectively; ω and I_0 represent the modulation frequency and the intensity of the incident light beam, respectively. Here, k_s and k_f denote the wave numbers inside and outside the PA source, respectively. Equation (1) can readily be solved for regular objects (e.g., sphere, infinite cylinder, layer, etc.). The solution is obtained by solving Eq. (1) in an appropriate coordinate system and by demanding continuity of pressure and normal component of particle velocity at the boundary [7]. This is referred to as the exact method. It does not have any restrictions on the size or strength of the inhomogeneity for its validity. The PA field at a point $\mathbf{r}$ (outside the source) for an infinite cylinder of radius a becomes [7]

$$\psi_{ex}(\mathbf{r}) = A\left[\frac{aJ_1(k_s a)H_0^1(k_f r)}{k_s a[J_1(k_s a)H_0^1(k_f a) - \hat{\rho}\hat{c}J_0(k_s a)H_1^1(k_f a)]}\right]. \tag{2}$$

Here, $A = i\mu\beta I_o v_s/C_p$; J and H^1 are the Bessel function and the Hankel function of first kind, respectively. The subscripts 0 and 1 denote the orders of each function. The dimensionless quantities are defined as $\hat{\rho} = \rho_s/\rho_f$ and $\hat{c} = v_s/v_f$. A schematic diagram is presented in Fig. 1(a). The subscript *ex* denotes the exact method. Equation (2) can also be used to yield the PA field generated by a solid circle/disk if we restrict ourselves to two dimensions. Equation (2) in the far field can be approximated as

$$\psi_{ex}(\mathbf{r}) \approx A\sqrt{\frac{2}{\pi k_f r}} \times \left[\frac{aJ_1(k_s a)e^{i(k_f r - \frac{\pi}{4})}}{k_s a[J_1(k_s a)H_0^1(k_f a) - \hat{\rho}\hat{c}J_0(k_s a)H_1^1(k_f a)]}\right]. \tag{3}$$

If the illuminated region consists of an ensemble of absorbing disks having the same opto-thermo-mechanical properties, Eq. (2) can be written in a generalized form as

$$\psi_{ex}(\mathbf{r}) = A\sum_{n=1}^{N} \times \left[\frac{a_n J_1(k_s a_n)H_0^1(k_f|\mathbf{r}-\mathbf{r}_n|)}{k_s a_n[J_1(k_s a_n)H_0^1(k_f a_n) - \hat{\rho}\hat{c}J_0(k_s a_n)H_1^1(k_f a_n)]}\right], \tag{4}$$

which in the far field reduces to

$$\psi_{ex}(\mathbf{r}) \approx A\sqrt{\frac{2}{\pi k_f r}} \times \sum_{n=1}^{N}\frac{1}{k_s a_n} \times \left[\frac{a_n J_1(k_s a_n)e^{i(k_f r - \frac{\pi}{4})}e^{-i\mathbf{k}_f\cdot\mathbf{r}_n}}{[J_1(k_s a_n)H_0^1(k_f a_n) - \hat{\rho}\hat{c}J_0(k_s a_n)H_1^1(k_f a_n)]}\right]. \tag{5}$$

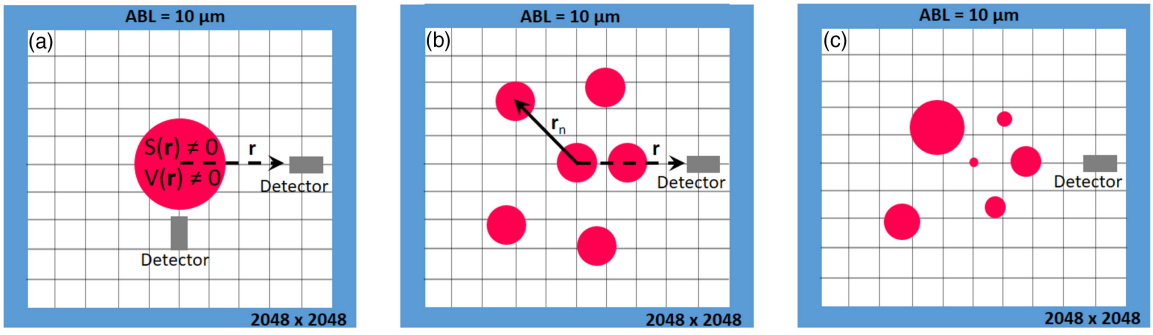

Fig. 1. (a) Schematic of the simulation setup for estimation of field produced by a single particle system. (b) and (c) Fields generated by a collection of monodisperse disks and an ensemble of polydisperse disks, respectively. ABL indicates the absorbing layer.

Here, $\mathbf{r}_n$ and a_n are the position vector and the radius of the nth source, respectively [see Fig. 1(b)]; the illuminated region contains N number of sources; $\mathbf{k}_f$ defines the direction of measurement. This is called the discrete particle approach, where the resultant PA field is simulated by adding the tiny fields produced by the individual particles.

In this work, the PA pressure in the near- and far-field regions have been estimated by numerically evaluating Eq. (2) for a homogeneous disk. Furthermore, Eq. (5) has been computed to obtain the PA fields generated by collections of monodisperse and polydisperse disks. The corresponding diagrams are displayed in Figs. 1(b) and 1(c), respectively.

B. Traditional Born Series

The PA wave equation as expressed in Eq. (1) can be rewritten, after some trivial manipulations, in a combined form as [5]

$$\nabla^2\psi(\mathbf{r}) + (k_f^2 + i\epsilon)\psi(\mathbf{r}) = -S(\mathbf{r}) - V(\mathbf{r})\psi(\mathbf{r}), \tag{6}$$

where ϵ is infinitesimally small real number and

$$S(\mathbf{r}) = \begin{cases} -\frac{i\mu\beta I_o\omega}{C_p}, & \text{if } |\mathbf{r}| \le a \\ 0, & \text{if } |\mathbf{r}| > a \end{cases}. \tag{7}$$

Similarly,

$$V(\mathbf{r}) = \begin{cases} k_s^2 - k_f^2 - i\epsilon, & \text{if } |\mathbf{r}| \le a \\ -i\epsilon, & \text{if } |\mathbf{r}| > a \end{cases}, \tag{8}$$

with $S(\mathbf{r})$ and $V(\mathbf{r})$ being the source term and the scattering potential, respectively. A representative diagram is shown in Fig. 1(a). The Green's function method can be employed to solve Eq. (6) yielding [4,5]

$$\psi(\mathbf{r}) = \int g(\mathbf{r}|\mathbf{r}_0)[V(\mathbf{r}_0)\psi(\mathbf{r}_0) + S(\mathbf{r}_0)]\mathrm{d}^3\mathbf{r}_0, \tag{9}$$

where $g(\mathbf{r}|\mathbf{r}_0)$ is the Green's function, and it is defined as the solution to

$$\nabla^2 g(\mathbf{r}|\mathbf{r}_0) + (k_f^2 + i\epsilon)g(\mathbf{r}|\mathbf{r}_0) = -\delta(\mathbf{r} - \mathbf{r}_0). \tag{10}$$

Here, δ is the Dirac delta function and the Green's function in the Fourier domain in terms of Fourier-transformed coordinates ($\mathbf{p}$) becomes

$$\tilde{g}(\mathbf{p}) = \frac{1}{(|\mathbf{p}|^2 - k_f^2 - i\epsilon)}. \tag{11}$$

Accordingly, the Green's function in the far field in two and three dimensions for a lossy unbounded medium can be derived as

$$g(\mathbf{r}|\mathbf{r}_0) \approx \frac{i}{4}\left(\frac{2}{\pi\sqrt{k_f^2 + i\epsilon}|\mathbf{r}|}\right)^{\frac{1}{2}} e^{i\left(\sqrt{k_f^2+i\epsilon}|\mathbf{r}-\mathbf{r}_0| - \frac{\pi}{4}\right)} \tag{12}$$

and

$$g(\mathbf{r}|\mathbf{r}_0) \approx \frac{e^{i\sqrt{k_f^2+i\epsilon}|\mathbf{r}-\mathbf{r}_0|}}{4\pi|\mathbf{r}|}, \tag{13}$$

respectively. Equations (12) and (13) demonstrate that the Green's function decays exponentially with distance for finite ϵ. This choice ensures that the function is localized and its total energy becomes finite also [5].

The convolution sum presented in Eq. (9) can be cast in the matrix form, yielding

$$\psi = GV\psi + GS, \tag{14}$$

where $G = F^{-1}\tilde{g}(\mathbf{p})F$, with F and F^{-1} being the forward and inverse Fourier transform operators, respectively. The recursive expansion of Eq. (14) provides

$$\psi_{\mathrm{TBS}} = [1 + GV + GVGV + \ldots]GS. \tag{15}$$

This infinite series converges if GV is less than unity [5]. The TBS method has been found to be efficient only for solving the inhomogeneous Helmholtz equation for small objects having weak scattering potential. Equation (15) has been evaluated herein to compute the PA fields for a variety of cases in two dimensions.

C. Convergent Born Series

Let us consider that both sides of Eq. (14) are multiplied by a preconditioner γ, providing [5]

$$\gamma\psi = \gamma GV\psi + \gamma GS. \tag{16}$$

It has been seen that such a step extends the validity domain of the TBS method, facilitating converging results for large structures as well [5]. Equation (16), after rearrangement of terms reduces to

$$\psi_{\mathrm{CBS}} = M\psi_{\mathrm{CBS}} + \gamma GS, \tag{17}$$

where $M = \gamma GV - \gamma + 1$. As in the previous case, an infinite series can be obtained by recursive expansion of Eq. (17) as

$$\psi_{\mathrm{CBS}} = [1 + M + M^2 + \ldots]\gamma GS, \tag{18}$$

requiring $M < 1$ for the convergence of the above infinite series. Furthermore, it converges for all structures if one chooses, $\gamma = \frac{i}{\epsilon}V(\mathbf{r})$ and $\epsilon \ge \max|k_s^2 - k_f^2|$ [5]. Equation (18) has been applied herein to compute the PA fields generated by different two dimensional systems containing a single particle and many particles, as shown in Fig. 1.

3. NUMERICAL METHODS

The performance of the TBS and CBS methods was examined by comparing the approximate and exact results for two-dimensional systems. Simulations involving two-dimensional systems are fast and also capable of providing useful insights about the efficacy of the techniques. For this purpose, a homogeneous disk with $a = 5$ μm was placed at the center of the computational domain. The speed of sound of the ambient medium was fixed at $v_f = 1500$ m/s. This numerical value is close to that of the extracellular matrix at room temperature [15]. Nevertheless, the speed of sound within the source was varied as $v_s = 1950$, 1800, 1650, 1500, 1350, and 1200 m/s. Therefore, the variation of the speed of sound mismatch parameter was restricted in this work to between 30% and −20%

with respect to that of the surrounding fluid medium. The PA fields were calculated at frequencies spanning from $f = 7.3$ to 2000 MHz, with an increment of 7.3 MHz. The corresponding wavelengths could be computed to be ≈ 205.5 to 0.75 μm, and the numerical values of wave number ($k_f = 2\pi f/v_f$) became $k_f = 0.03$ to $8.38\ \mu m^{-1}$. Optical and thermo-mechanical parameters for the PA source were set to unity ($I_0 = 1$, $\mu = 1$, $\beta = 1$, $C_p = 1$) [15]. Such a choice would control the amplitude of the PA field, but would not affect its spectral features. The density of the medium inside the PA source was considered to be the same as that of the outside, $\rho_s = \rho_f = 1000\ kg/m^3$. The PA fields were computed at a point close to the source (at a distance 10 μm from the center of the source) as well as far away from the source (at a distance 75 μm). The PA field produced by a single disk was obtained by evaluating Eq. (2) for the exact method.

The size of the two-dimensional system was taken as 2048×2048 with a pixel size of 100 nm (see Fig. 1) in order to obtain the PA fields provided by the TBS and CBS approaches. At first, Eqs. (7) and (8) were evaluated to generate the spatial map of $S(\mathbf{r})$ and $V(\mathbf{r})$, respectively. The numerical values of Green's function were also determined at the grid points in the frequency domain [Eq. (11)]. Initial pressure values were taken as

$$\psi_{TBS_0}(\mathbf{r}) = \text{ifft}_2[\tilde{g}(\mathbf{p})\text{fft}_2 S(\mathbf{r})] \tag{19}$$

and

$$\psi_{CBS_0}(\mathbf{r}) = \gamma(\text{ifft}_2[\tilde{g}(\mathbf{p})\text{fft}_2 S(\mathbf{r})]) \tag{20}$$

for the two approaches, respectively. The notations fft_2 and ifft_2 stand for the forward and inverse fast Fourier transforms in two dimensions, respectively. Moreover, all the multiplications were performed elementwise. After that, iterative computations were carried out. The pressure data for the TBS and CBS algorithms were generated in the following manners:

$$\psi_{TBS_{n+1}}(\mathbf{r}) = \text{ifft}_2[\tilde{g}(\mathbf{p})\text{fft}_2[V(\mathbf{r})\psi_{TBS_n}(\mathbf{r}) + S(\mathbf{r})]] \tag{21}$$

and

$$\psi_{CBS_{n+1}}(\mathbf{r}) = \psi_{CBS_n}(\mathbf{r}) - (i/\epsilon)V(\mathbf{r})(\psi_{CBS_n}(\mathbf{r}) - \text{ifft}_2[\tilde{g}(\mathbf{p})\text{fft}_2[V(\mathbf{r})\psi_{CBS_n}(\mathbf{r}) + S(\mathbf{r})]]), \tag{22}$$

respectively. Here, n is the iteration number. After each iteration, the total error along the center line was calculated as

$$\text{Total error} = \sum_{m=1}^{2048} \frac{|\psi_{n+1}(1024, m) - \psi_n(1024, m)|}{|\psi_n(1024, m)|}. \tag{23}$$

We assumed that the steady state was reached if the total error was less than 10^{-4}. The iterative calculation stopped once the steady state was reached or after 2000 steps, whichever was earlier.

It might be noted here that the PA waves at each boundary were absorbed within a region (with thickness spanning 100 grid points) called the absorbing layer (ABL). This layer greatly reduced the amplitudes of the reflected waves. Essentially, each wave in the boundary layer was dampened exponentially with a decay constant $\sqrt{\epsilon}$, which was arbitrarily chosen. An attenuation mask was used for this purpose, such as

$$AtnMsk(\mathbf{r}) = \begin{cases} e^{-\sqrt{\epsilon}|\mathbf{r}|}, & \text{if } |\mathbf{r}| \text{ lies within the ABL} \\ 1, & \text{otherwise.} \end{cases} \tag{24}$$

Therefore, after each iteration, the pressure field was updated as $\psi_n = AtnMsk\psi_{n+1}$. The updated ψ_n was inserted into Eq. (21) as an input, and then the new ψ_{n+1} was estimated. The same steps were also followed for the CBS method. It might be further mentioned here that the convolution sums in Eqs. (21) and (22) were evaluated via a fast Fourier transform, which inherently implements the periodic boundary conditions. In other words, it causes waves leaving from one boundary to reappear from the opposite boundary. This effect can be suppressed by wrapping the computational domain with an absorbing layer. The attenuation mask serves this purpose. It seemed to be a very crucial step in order to obtain accurate estimates of the PA field.

In this work, the role of ϵ on the convergence of the PA field in different methods was investigated first. Accordingly, the numerical values of ϵ were chosen to be $\epsilon = 0.6k_f^2$ and $0.8k_f^2$. However, in all other computations, ϵ was taken as $\epsilon = 0.8k_f^2$. In fact, $\max|k_s^2 - k_f^2|$ could be computed to be $0.41k_f^2$, $0.31k_f^2$, $0.17k_f^2$, 0, $0.23k_f^2$, and $0.56k_f^2$ when v_s was varied from 1950 to 1200 m/s. Therefore, both the values of ε satisfied $\epsilon \geq \max|k_s^2 - k_f^2|$. It might be noted that Osnabrugge *et al.* also used $\epsilon = 0.8k_f^2$ in their work [5]. The numerical algorithm is presented in detail in [11]. The numerical code was written in a Matlab environment, and can be found at [16]. The code was executed in a high-performance virtual machine [CentOS, Intel Core Processor (Broadwell, IBRS) working at 2.19 GHz, 128 GB RAM, 40 Cores].

In order to develop better insights regarding the robustness of the TBS and CBS algorithms, we also calculated and compared the PA fields generated by the two-dimensional systems consisting of monodisperse and polydisperse disks as shown in Figs. 1(b) and 1(c), respectively. Essentially, six disks were placed randomly within each numerical phantom. The radius and position coordinates of each disk are presented in Table 1. The density and the speed of sound of the PA sources

Table 1. Radii and Position Coordinates of the Disks Considered in Many-Particle Systems

Many-Particle System	a (μm)	x (μm)	y (μm)
Monodisperse Disks	5	0	0
	5	−23.5	17.5
	5	−32.5	−32.5
	5	7.5	−22.5
	5	19.5	0
	5	12.5	18.5
Polydisperse Disks	2	0	0
	22	−22.5	17.5
	15	−32.5	−32.5
	6	7.5	−22.5
	11	17	0
	2	12.5	18.5

were taken to be the same as that of the surrounding medium (i.e., $\rho_s = \rho_f = 1000$ kg/m^3 and $v_s = v_f = 1500$ m/s).

4. NUMERICAL RESULTS

A. Convergence of Pressure Field

Plots of the real part of $\psi(\mathbf{r})$ with distance from the center of the source at $f \approx 102$ MHz after some specific iterations are given in Fig. 2, in order to study how the pressure field expands with iteration. The pressure fields were calculated at $\epsilon = 0.8k_f^2$ and $0.6k_f^2$ for both the TBS and CBS protocols. Figures 2(a)–2(c) display that the pressure field expands gradually as the iteration proceeds, and finally reaches the steady state. For example, the pressure field only remains non-zero in the proximal regions of the source after the first iteration [see Fig. 2(a)]. However, the pressure field builds up outside the source region after the fifth iteration. The propagation speed of the PA field is higher for $\epsilon = 0.6k_f^2$ in comparison to that of $0.8k_f^2$. For instance, more fluctuations can be observed in the distal regions from the source for $\epsilon = 0.6k_f^2$ than that of the $0.8k_f^2$ [see blue line compared to magenta circles in Fig. 2(b)]. Further, as expected, pressure data attain steady state after the 75th and 114th iterations for the lower and higher values of ϵ, respectively [see Fig. 2(c)]. Therefore, the smaller the value of ϵ, the faster is the convergence. The corresponding plots for the CBS technique are given in Figs. 2(d)–2(f), and analogous observations can be made.

B. Single-Particle System

1. Near Field

Figure 3 shows the variation of the pressure field as a function of frequency over a large bandwidth (7–2000 MHz) at different speed of sound mismatch conditions when the solutions were shouted in the near field. The corresponding pressure field provided by the exact method is also plotted for comparison. The variation of the size parameter ($k_f a$) for the entire frequency range is presented along the top x axis in Figs. 3(a) and 3(f). The curves exhibit the well-known peaks and dips pattern. The number of oscillations increased as v_s was decreased from 1950 to 1200 m/s. Both the TBS and CBS methods exhibit good agreement with the exact result over the entire frequency/size parameter range [see Figs. 3(b)–3(e)]. The location and depth of the minima (also heights of the maxima) are well reproduced by the TBS and CBS methods, as evident from these figures. Figures 3(a)–3(f) demonstrate that the CBS method provides accurate fits to the exact curves. However, the TBS curves demonstrate large deviation compared to the exact method as shown in Figs. 3(a) and 3(f). It grows nonlinearly as the frequency/size parameter increases (scale along the right y axis). The nonlinear behavior distinctively appears at $k_f a > 25$ in Fig. 3(a) and $k_f a > 9$ in Fig. 3(f).

2. Far Field

Figure 4 illustrates how the PA pressure varies with frequency over the same bandwidth at different speed of sound contrast settings. The PA pressure was computed at a large distance (75 μm) from the source. Similar graphs were also presented in [11]. The curves demonstrate similar trends as observed in Fig. 3. However, the magnitude of the PA pressure at each frequency is less than that of Fig. 3. This is due to the fact that the pressure field falls off with distance (i.e., $1/\sqrt{r}$ in two dimensions). As in the previous case, converging solutions for the TBS method have been obtained up to $k_f a \approx 25$ in Fig. 4(a) and $k_f a \approx 9$ in Fig. 4(f). The CBS method remains valid in the entire range of speed of sound mismatch considered in this study.

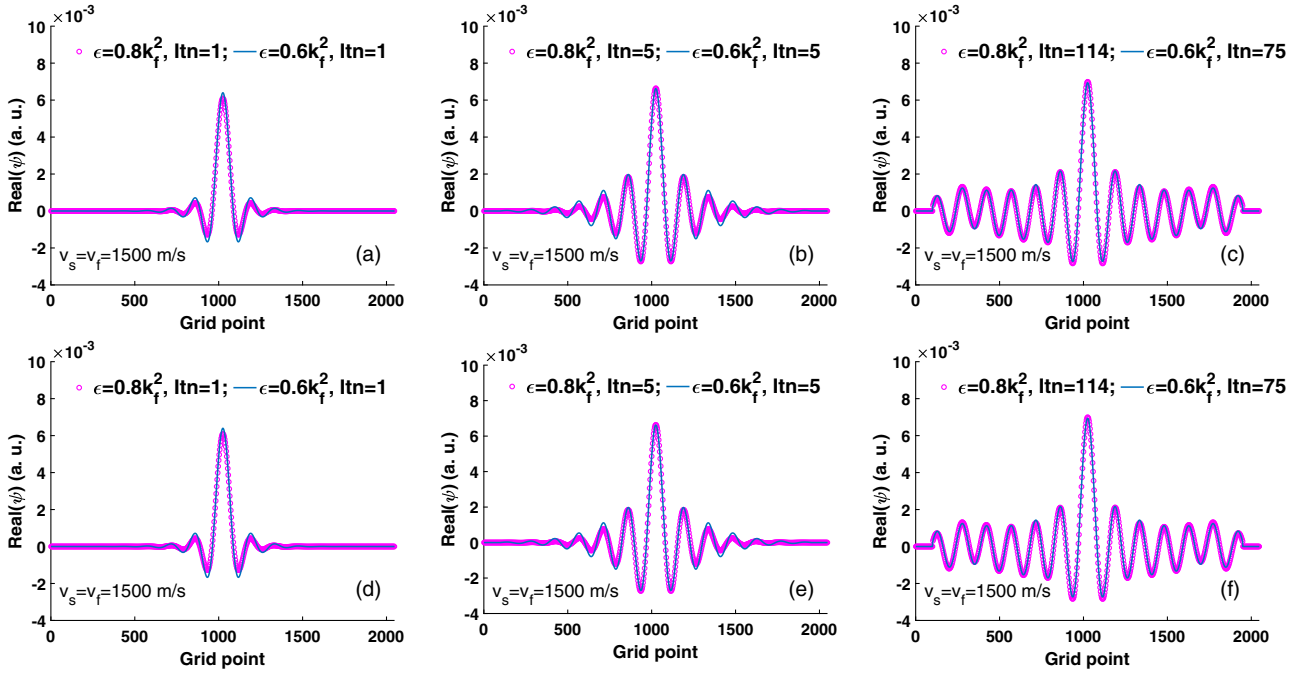

Fig. 2. (a)–(c) Variation of real part of ψ at ≈ 102 MHz along the central line for a single PA source after some specific iterations for the TBS method at two particular values of ϵ. (d)–(f) Same as (a)–(c) but for the CBS method. Itn means iteration.

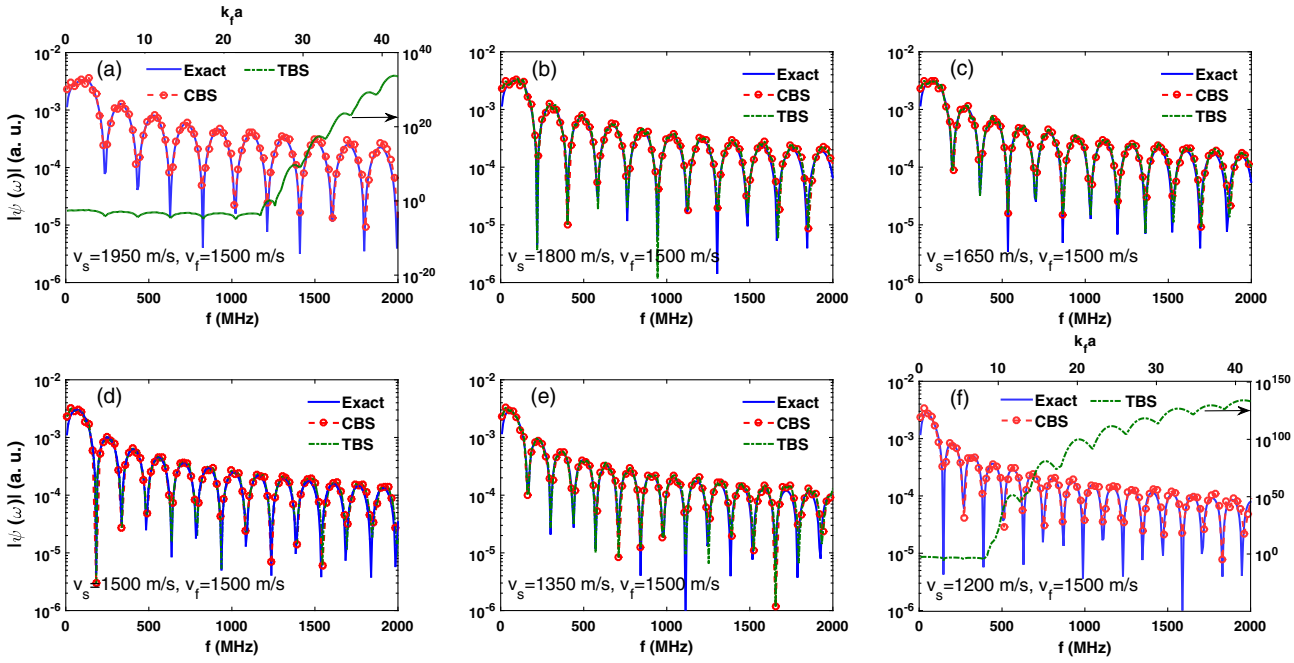

Fig. 3. (a)–(f) Variation of the PA pressure in the near field (emitted by a disk of 5 μm radius) with frequency. The solid line, dash-dot-dash line, and dash-dash line with marker O are for the exact, TBS, and CBS methods, respectively. The corresponding change of the size parameter ($k_f a$) is presented at the top x axis in (a) and (f). The distance of the detector from the center of the source was 10 μm. The scale for the TBS method in (a) and (f) is shown along the right y axis.

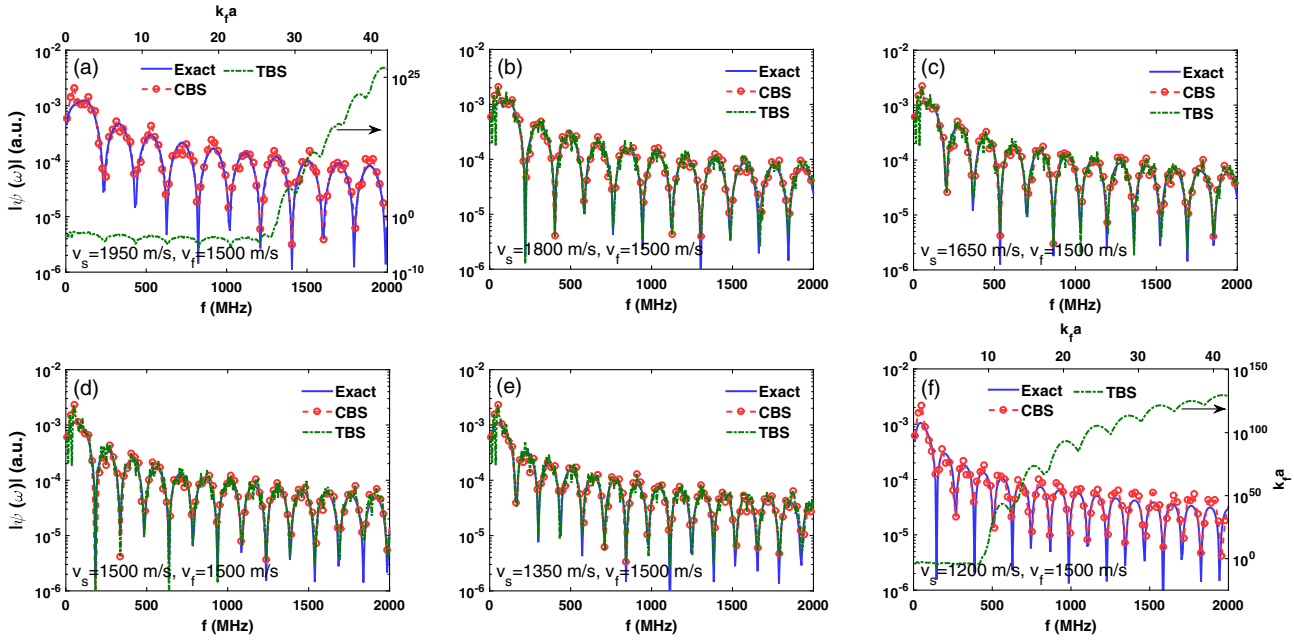

Fig. 4. (a)–(f) Plots of the PA fields computed at the far field as a function of frequency for a source with 5 μm radius. The corresponding change of the size parameter ($k_f a$) is presented at the top x axis in (a) and (f). The detector was placed at a distance 75 μm from the center of the source. The scale for the TBS method in (a) and (f) is drawn along the right y axis.

C. Many-Particle Systems

1. Monodisperse Disks

The PA field from a collection of monodisperse disks has been calculated for a point detector situated at a large distance from the center of the computational domain. Computed PA fields are shown in Figs. 5(a) and 5(b) for the TBS and CBS algorithms, respectively. Two separate graphs have been used for this purpose to increase the clarity of the graphs. The PA pressure data for the exact method are also included in each figure as a ready reference. Figures 5(a) and 5(b) in general appear as Fig. 4(d), meaning that they retain the spectral features of a

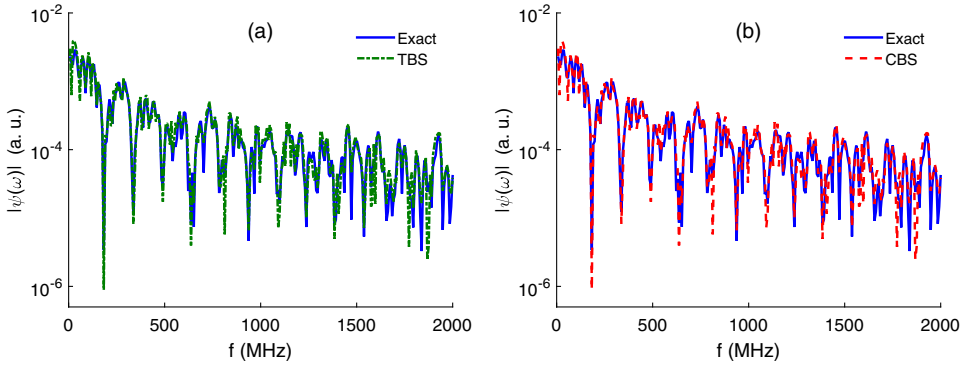

Fig. 5. (a) Plots of the PA field calculated in the far field for a collection of monodisperse disks for the exact and TBS methods. (b) Same as (a) but for the CBS approach.

source of radius 5 μm. For example, the locations of the minima appear at the same frequencies as those of Fig. 4(d). However, the curves in Fig. 5 are not as smooth as those of Fig. 4(d). Small fluctuations exist over the entire frequency range. This is because of the interference of the waves coming from multiple disks. The interference pattern is superimposed with the single particle spectrum. It may be noted that the amplitudes of fluctuations are not prominent up to approximately 1200 MHz; nevertheless, they become comparable to the heights of the peaks and depths of the dips of the single particle graph at higher frequencies.

2. Polydisperse Disks

The PA spectra for a system comprised of multiple particles with size dispersity are shown in Fig. 6 for the three methods. The PA field was calculated at a large distance from the center of the computational region. The density and speed of sound inside and outside the PA sources were considered to be the same as mentioned earlier. The plots for the TBS and CBS techniques are presented in two separate figures in order to improve the visibility of subtle changes. It is evident from Fig. 6 that the strength of the PA field is greater than that of Fig. 5 at least in the lower frequency regime (<100 MHz). This is because of the presence of bigger PA sources. The PA spectra do not show regularly spaced maxima and minima which are present in the previous figures [see Fig. 5]. Further, each spectrum demonstrates prominent and rapid fluctuations owing to the fact that the illuminated region encloses sources with nonuniform sizes. Note that the resultant spectrum is the superposition of such spectra from sources with different sizes. Finally, the computed spectra for the TBS and CBS methods exhibit good agreement with the exact result over the entire frequency range, confirming that the Born series methods can be deployed to estimate the PA field generated by an ensemble of polydisperse light-absorbing structures.

5. DISCUSSION AND CONCLUSIONS

The Born series methods, known as the TBS and CBS schemes, have been deployed in this work to solve the time-independent inhomogeneous PA wave equation. The source term of this equation has two parts. The first part appears because of the conversion of optical energy into pressure wave via the PA effect. It becomes a constant for an optically homogeneous source and for uniform illumination. It is easy to find out an analytical (regular shapes) or numerical (irregular objects) solution to the PA wave equation when it retains this part only. The second part arises when the speed of sound within the source region differs from that of the surrounding medium. It essentially acts as a scattering potential. It behaves as a potential well when $v_s > v_f$ (or $k_s < k_f$) and as a potential barrier when $v_s < v_f$ (or $k_s > k_f$). The contribution of this part to the final solution

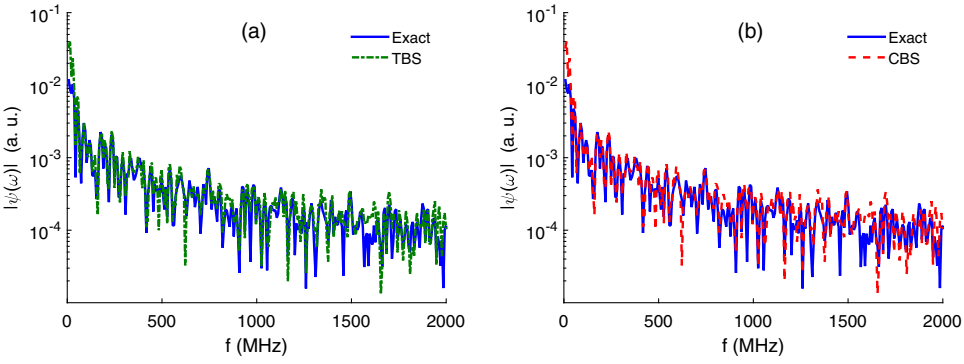

Fig. 6. (a) Variation of the PA fields (far away from the source) as a function of frequency for the exact and the TBS methods when the computational region contains six arbitrarily positioned disks with size dispersity. (b) Same as (a) but for the CBS algorithm.

can be found out if the pressure field inside the source is known. Obtaining a converging solution for this part is not trivial, and an iterative approach is generally applied for this purpose.

It may be noted that in this formulation [Eq. (6)], scattering potential for an acoustically homogeneous source becomes nonzero (i.e., $V = -i\epsilon$) for nonvanishing ϵ. For such a case, the solution has to be obtained iteratively. The solution grows with iteration because of V whereas it decays because of the Green's function. These two factors essentially balance each other, and that is why both the TBS and CBS solutions exhibit good agreement with the exact solution [see Figs. 3(d) and 4(d)].

The TBS method converges very fast for low-frequency waves [see Fig. 7(a)]. However, it takes longer for high-frequency waves. For instance, it converged within approximately 100 iterations up to 100 MHz, but nearly 350 steps were required at 500 MHz when $v_s = v_f = 1500$ m/s. The number of iterations did not differ much when contrast in the speed of sound was varied. Moreover, it was observed that the number of iterations required for convergence followed approximately the same pattern as that of the PA spectrum [see Figs. 3 and 4]. It means that the number of iterations needed for convergence was greater for maxima locations compared to that of minima positions. The CBS algorithm took the same number of steps as that of the TBS technique at any frequency for convergence. Nevertheless, the execution time for the CBS method at each frequency was longer because more matrix operations were performed than the TBS protocol, as shown in Fig. 7(b). It was found that lower the value of ϵ, the faster the convergence was for both the methods. However, the lower bound of ϵ has to satisfy $\epsilon \geq \max|k_s^2 - k_f^2|$ for the CBS technique. Additionally, the computation time required for PA field calculation using the Born series and the k-Wave methods needs to be compared in the future.

It is clear from Eq. (2) that the exact approach takes care of the mismatch in the density between the source and the surrounding medium while solving the problem, whereas it is not included in Eq. (6). We investigated this aspect as well in this work. Figure 8 illustrates how the PA fields vary with frequency when the density of the source region was varied within ±10% with respect to the ambient medium. The speed of sound was set to be constant for both media (i.e., $v_s = v_f = 1500$ m/s). The PA pressure data for the CBS technique was not included

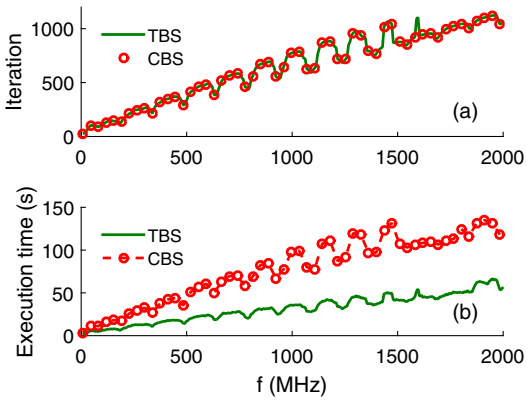

Fig. 7. (a) Plots of number of iterations required for convergence versus frequency for the TBS and CBS methods when $v_s = v_f = 1500$ m/s. (b) Plots of execution time needed for convergence versus frequency.

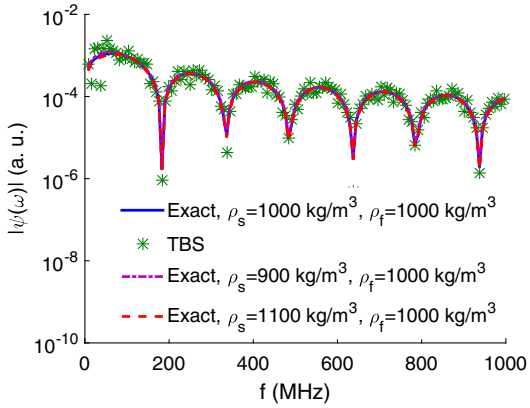

Fig. 8. Demonstration of the PA fields far away from the source and generated by the exact and TBS methods as a function of frequency for a series of density mismatch settings when $v_s = v_f = 1500$ m/s.

in this figure since both the iterative methods become the same when $v_s = v_f$. The scale of the x axis was limited to 1000 MHz in order to improve the clarity of the figure. It can be seen from Fig. 8 that plots for the exact method are not visibly distinguishable from those of the TBS technique, establishing that the density mismatch has less impact on the PA field than the speed of sound contrast. Therefore, the Born series method may be applied even if the difference in density between the source and the ambient medium is up to ±10%.

The Born series methods were also utilized in this work to estimate the PA field generated by a collection of sources. The corresponding simulation results for the TBS and CBS techniques exhibited good agreement with the exact results. It might be mentioned here that for this case, we considered $v_s = v_f = 1500$ m/s in order to avoid multiple scattering of the PA waves. It appears that the Born series framework can be employed as well to study the effect of multiple scattering of acoustic waves. In that case, $v_s \neq v_f$. We plan to address this issue in the future. It might also be interesting to examine how the CBS would work for large acoustic inhomogeneity (e.g., bone–tissue interface).

In conclusion, in this work, we employed the Born series methods to solve the time-independent inhomogeneous PA wave equation. The inhomogeneity term originating from contrast in the speed of sound between the source and the surrounding medium was included within the wave equation. The performance of the Born series methods has been examined by numerically calculating the PA field generated by a homogeneous disk, and then by comparing it with the exact result. The accuracy of these techniques in estimating the PA field produced by an ensemble of disks (monodisperse/polydisperse) was also assessed. The TBS scheme was found to reproduce the exact results for sufficiently large objects (up to $k_f a = 42$) when the contrast in the speed of sound was limited from $> -11\%$ to $<22\%$. The validity domain of the Born series method was further extended by the CBS algorithm, which could provide accurate results even when the contrast in the speed of sound was varied from −20% to 30%. The methods as well as numerical findings should be valid in the case of similar problems in acoustics. Our simulation results suggest that the CBS protocol may be applied in practice to obtain the numerical solution to the

inhomogeneous PA wave equation for a source having arbitrary size and shape, and sufficiently large scattering strength.

Acknowledgment. The computational results reported in this work were performed on the Central Computing Facility of IIITA, Allahabad. RKS would like to thank Sreedevi Gutta of MIG, IISc for her help. The author also thanks Anuj Kaushik and Avijit Paul for proofreading the paper.

Disclosures. The authors declare no conflicts of interest.

REFERENCES

1. M. C. W. Van Rossum and T. M. Nieuwenhuizen, "Multiple scattering of classical waves: microscopy, mesoscopy and diffusion," Rev. Mod. Phys. **71**, 313–373 (1993).
2. J. Schäfer and A. Kienle, "Scattering of light by multiple dielectric cylinders: comparison of radiative transfer and Maxwell theory," Opt. Lett. **33**, 2413–2415 (2008).
3. C. F. Bohren and D. R. Huffman, *Absorption and Scattering of Light by Small Particles* (Wiley-VCH, 1998).
4. P. M. Morse and H. Feshbach, *Methods of Theoretical Physics* (McGraw-Hill, 1953), pp. 791–895.
5. G. Osnabrugge, S. Leedumrongwatthanakun, and I. M. Vellekoop, "A convergent Born series for solving the inhomogeneous Helmholtz equation in arbitrarily large media," J. Comput. Phys. **322**, 113–124 (2016).
6. B. Krüger, T. Brenner, and A. Kienle, "Solution of the inhomogeneous Maxwell's equations using a Born series," Opt. Express **21**, 25165–25182 (2017).
7. G. J. Diebold, T. Sun, and M. I. Khan, "Photoacoustic monopole radiation in one, two and three dimensions," Phys. Rev. Lett. **67**, 3384–3387 (1991).
8. B. E. Treeby and B. T. Cox, "k-wave: MATLAB toolbox for the simulation and reconstruction of photoacoustic wave fields," J. Biomed. Opt. **15**, 021314 (2010).
9. N. Baddour, "Theory and analysis of frequency-domain photoacoustic tomography," J. Acoust. Soc. Am. **123**, 2577–2590 (2008).
10. N. Baddour and A. Mandelis, "The effect of acoustic impedance on subsurface absorber geometry reconstruction using 1D frequency-domain photoacoustics," Photoacoustics **3**, 132–142 (2015).
11. A. Kaushik, P. K. Yalavarthy, and R. K. Saha, "Convergent Born series improves accuracy of numerical solution of time independent photoacoustic wave equation," J. Mod. Opt. **67**, 849–855 (2020).
12. R. K. Saha, S. Karmakar, A. Adhikari, and M. C. Kolios, "Photoacoustic field calculation for nonspherical axisymmetric fluid particles," Biomed. Phys. Eng. Express **3**, 015017 (2017).
13. A. Kaushik, D. Sonker, and R. K. Saha, "Study on angular distribution of differential photoacoustic cross-section and its implication in source size determination," J. Opt. Soc. Am. A. **36**, 387–396 (2019).
14. A. Kaushik, A. Paul, and R. K. Saha, "A systematic analysis of frequency dependent differential photoacoustic cross-section data for source size estimation," J. Opt. Soc. Am. A **37**, 1895–1904 (2020).
15. R. K. Saha and M. C. Kolios, "A simulation study on photoacoustic signals from red blood cells," J. Acoust. Soc. Am. **129**, 2935–2943 (2011).
16. https://github.com/ratanksaha/Photoacoustic-field-calculation.